

Opto-acoustic behavior of coated fiber Bragg gratings

Massimo Moccia,¹ Marco Pisco,¹ Antonello Cutolo,¹ Vincenzo Galdi,²
Pierantonio Bevilacqua,³ and Andrea Cusano^{1,*}

¹Optoelectronic Division, Department of Engineering, University of Sannio, Corso Garibaldi 107,
I-82100 Benevento, Italy

²CNR-SPIN and Waves Group, Department of Engineering, University of Sannio, Corso Garibaldi 107,
I-82100 Benevento, Italy

³Withthead Alenia Sistemi Subacquei (WASS), via Monteruscello 75, Pozzuoli (Na), Italy
[*a.cusano@unisannio.it](mailto:a.cusano@unisannio.it)

Abstract: In this paper, we present the study of the acousto-optic behavior of underwater-acoustic sensors constituted by fiber Bragg gratings (FBGs) coated by ring-shaped overlays. Via full-wave numerical simulations, we study the complex opto-acousto-mechanical interaction among an incident acoustic wave traveling in water, the optical fiber surrounded by the ring shaped coating, and the FBG inscribed the fiber, focusing on the frequency range 0.5-30 kHz of interest for SONAR applications. Our results fully characterize the mechanical behavior of an acoustically driven coated FBG, and highlight the key role played by the coating in enhancing significantly its sensitivity by comparison with a standard uncoated configuration. Furthermore, the hydrophone sensitivity spectrum exhibits characteristic resonances, which strongly improve the sensitivity with respect to its background (i.e., away from resonances) level. Via a three-dimensional modal analysis, we verify that the composite cylindrical structure of the sensor acts as an acoustic resonator tuned at the frequencies of its longitudinal vibration modes. In order to evaluate the sensor performance, we also carry out a comprehensive parametric analysis by varying the geometrical and mechanical properties of the coating, whose results also provide a useful design tool for performance optimization and/or tailoring for specific SONAR applications. Finally, a preliminary validation of the proposed numerical analysis has been carried out through experimental data obtained using polymeric coated FBGs sensors revealing a good agreement and prediction capability.

©2011 Optical Society of America

OCIS codes: (060.3735) Fiber Bragg gratings; (060.2370) Fiber optics sensors; (280.4788) Optical sensing and sensors, (230.1040) Acousto-optical devices.

References and links

1. C. K. Kirkendall and A. Dandridge, "Overview of high performance fibre-optic sensing," *J. Phys. D Appl. Phys.* **37**(18), R197–R216 (2004).
2. E. Udd, *Fiber Optic Sensors: An Introduction for Engineers and Scientists* (Wiley, New York, 1990).
3. G. Wild and S. Hinckley, "Acousto-ultrasonic optical fiber sensors: Overview and state-of-the-art," *IEEE Sens. J.* **8**(7), 1184–1193 (2008).
4. D. J. Hill and P. J. Nash, "In-water acoustic response of a coated DFB fibre laser sensor," *Proc. SPIE* **4185**, 33–36 (2000).
5. S. Fosters, A. Tikhomirova, M. Milnesa, J. van Velzena, and G. Hardyb, "A fibre laser hydrophone," *Proc. SPIE* **5855**, 627–630 (2005).
6. S. Goodman, S. Foster, J. Van Velzen, and H. Mendis, "Field demonstration of a DFB fibre laser hydrophone seabed array in Jervis Bay, Australia," *Proc. SPIE* **7503**, 75034L1 (2009).
7. N. Takahashi, A. Hirose, and S. Takahashi, "Underwater acoustic sensor with fiber Bragg grating," *Opt. Rev.* **4**(6), 691–694 (1997).
8. N. Takahashi, K. Yoshimura, S. Takahashi, and K. Imamura, "Development of an optical fiber hydrophone with fiber Bragg grating," *Ultrasonics* **38**(1-8), 581–585 (2000).

9. W. Thongnum, N. Takahashi, and S. Takahashi, "Temperature stabilization of fiber Bragg grating vibration sensor," in *OFS 2002, 15th Optical Fiber Sensors Conference Technical Digest, 2002*. (2002), Vol. 1, pp. 223–226.
10. N. Takahashi, K. Tetsumura, and S. Takahashi, "Multipoint detection of acoustical wave in water with WDM fiber Bragg grating sensor," *Proc. SPIE* **3740**, 270–273 (1999).
11. H. Yokosuka, S. Tanaka, and N. Takahashi, "Time-division multiplexing operation of temperature-compensated fiber Bragg grating underwater acoustic sensor array with feedback control," *Acoust. Sci. Technol.* **26**(5), 456–458 (2005).
12. D. J. Hill and G. A. Cranch, "Gain in hydrostatic pressure sensitivity of coated fiber Bragg grating," *Electron. Lett.* **35**(15), 1268–1269 (1999).
13. Y. Liu, Z. Guo, Y. Zhang, K. S. Chiang, and X. Dong, "Simultaneous pressure and temperature measurement with polymer-coated fiber Bragg grating," *Electron. Lett.* **36**(6), 564–566 (2000).
14. G. B. Hocker, "Fiber optic acoustic sensors with composite structure: an analysis," *Appl. Opt.* **18**(21), 3679–3683 (1979).
15. A. Cusano, S. D'Addio, A. Cutolo, S. Campopiano, M. Balbi, S. Balzarini, and M. Giordano, "Enhanced acoustic sensitivity in polymeric coated fiber Bragg grating," *Sensors Transducers* **82**, 1450–1457 (2007).
16. S. Campopiano, A. Cutolo, A. Cusano, M. Giordano, G. Parente, G. Lanza, and A. Laudati, "Underwater acoustic sensors based on fiber Bragg gratings," *Sensors (Basel Switzerland)* **9**(6), 4446–4454 (2009).
17. L. D. Landau and E. M. Lifshitz, *Fluid Mechanics* (Pergamon Press, 1987).
18. F. Ihlenburg, *Finite Element Analysis of Acoustic Scattering* (Springer, 1998).
19. S. Timoshenko and J. N. Goodier, *Theory of Elasticity* (McGraw-Hill, 1951).
20. C. J. S. de Matos, P. Torres, L. C. G. Valente, W. Margulis, and R. Stubbe, "Fiber Bragg grating (FBG) characterization and shaping by local pressure," *J. Lightwave Technol.* **19**(8), 1206–1211 (2001).
21. A. Minardo, A. Cusano, R. Bernini, L. Zeni, and M. Giordano, "Response of fiber Bragg gratings to longitudinal ultrasonic waves," *IEEE Trans. Ultrason. Ferroelectr. Freq. Control* **52**(2), 304–312 (2005).
22. COMSOL Multiphysics, *User's Guide* (COMSOL AB, 2008).
23. U. Fano, "Effects of configuration interaction on intensities and phase shifts," *Phys. Rev.* **124**(6), 1866–1878 (1961).
24. K. Sakoda, "Symmetry, degeneracy, and uncoupled modes in two-dimensional photonic lattices," *Phys. Rev. B Condens. Matter* **52**(11), 7982–7986 (1995).
25. A. Ricciardi, I. Gallina, S. Campopiano, G. Castaldi, M. Pisco, V. Galdi, and A. Cusano, "Guided resonances in photonic quasicrystals," *Opt. Express* **17**(8), 6335–6346 (2009).
26. G. M. L. Gladwell and D. K. Vijay, "Natural frequencies of free finite length circular cylinders," *J. Sound Vibrat.* **42**(3), 387–397 (1975).
27. C. F. Beards, *Structural Vibration Analysis and Damping* (Butterworth Heinemann, 1996).
28. A. Guran, J. Ripoché, and F. Ziegler, *Acoustic Interactions with Submerged Elastic Structures* (World Scientific, 1996).
29. M. Moccia, M. Pisco, A. Cutolo, V. Galdi, and A. Cusano, "Resonant hydrophones based on coated fiber Bragg gratings. Part I: numerical analysis," *Proc. SPIE* **7753**, 775384, 775384-4 (2011).
30. M. Moccia, M. Consales, A. Iadicicco, M. Pisco, M. Giordano, A. Cutolo, and A. Cusano, "Resonant hydrophones based on coated fiber Bragg gratings. Part II: experimental analysis," *Proc. SPIE* **7753**, 775383, 775383-4 (2011).
31. "Damival resins: polyurethane and epoxy systems for potting and encapsulation," www.sibel.bg/upl_doc/DAMIVAL_E.pdf.
32. "Huntsman advanced materials," www.huntsmanservice.com/Product_Finder/ui/PSDetailCompositeList.do?pInfoSBUID=9&PCId=1663
33. "eFunda polymer material properties," http://www.efunda.com/materials/polymers/properties/polymer_datasheet.cfm?MajorID=PU&MinorID=1.
34. T. Pritz, "The Poisson's loss factor of solid viscoelastic materials," *J. Sound Vibrat.* **306**(3-5), 790–802 (2007).
35. A. Sorathia, "Polyurethane-epoxy interpenetrating polymer network acoustic damping material," U.S. Patent No. 5,331,062 (19 July 1994).
36. F. A. Khayyat and P. Stanley, "The dependence of the mechanical, physical and optical properties of Araldite CT200/HT 907 on temperature over the range –10°C to 70°C," *J. Phys. D Appl. Phys.* **11**(8), 1237–1247 (1978).
37. F. J. P. Chaves, "Application of adhesive bonding in PVC windows," MSc Thesis (University of Porto, Portugal, 2005), <http://www.scribd.com/doc/37203644/MSc-Thesis>.
38. Bodo Möller Chemie, "Technical data: PUR and epoxy" http://www.bm-chemie.de/content/de/download/pub/Elektrogiessharze_12_03_2009.pdf

1. Introduction

Acoustic sensors are widely used in civilian and military applications as SONAR devices. The best established technology relies on piezo ceramic (lead zirconate titanate—PZT) hydrophones which convert an acoustic wave into an output voltage directly related to the wave amplitude. Consequently, part of the electronics for the multiplexing and the related telemetry is immersed in water (and hence subjected to continuous harm and degradation) and

is rather heavy and bulky because of the wiring. The scenario becomes even harsher when taking into account the water infiltrations which often occur during medium and long term explorations, with the consequent detrimental effects of performance degradation and malfunctioning.

In recent years, optical technology developments have demonstrated that optical sensors can be used as acoustic detectors in a wide frequency range: from SONAR applications to ultrasonic imaging [1–3]. Acousto-optic sensors have the advantage of compact size, in addition to electromagnetic interference immunity, stability in harsh environments, and multiplexing capability [3].

Several sensing configurations have been proposed which rely on optical technology for acoustic detection in underwater scenarios. A promising approach was proposed by Hill *et al.* [4], by using a distributed feedback fiber laser (DFB FL) as sensing element. The frequency of light produced by the DFB FL was extremely sensitive to acoustic perturbations. In [5], Foster *et al.* obtained a sensitivity of 100 nm/MPa by using a metal housing for the DFB FL sensor in order to enhance the hydrophone response. Even though DFB FL provides respectable sensitivities, and in-field demonstration of an FL hydrophone array has been also recently reported [6], sophisticated technologies are needed.

Simpler approaches have been proposed based on the use of fiber Bragg gratings (FBGs) in standard optical fibers for acoustic detection. Optical sensors based on FBG indeed demonstrated significant performance as underwater acoustic sensors by exploiting relatively cheap and well-established methodologies and technologies (i.e., multiplexing strategies, interrogation units, etc.) already developed for various FBG communication and sensing applications. In [7] and [8], Takahashi *et al.* proposed a simple in-fiber FBG as underwater acoustic detector. The operational range and the pressure sensitivity of the hydrophone were systematically investigated [7], and the frequency response was studied in various acoustic frequency ranges [8]. Improvements in the hydrophone response were obtained via temperature compensation [9] by using feedback control. Multiplexing operation with FBG hydrophones with both time and wavelength division strategies was demonstrated in [10] and [11], respectively, in order to enable for multipoint detection.

The main limitation to the performance of FBG-based sensors in underwater applications stems from the high value (about 72 GPa) of the elastic (Young's) modulus of the glass constituting the optical fiber. This was also the limiting factor for the application of FBGs as hydrostatic pressure sensors. In this framework, Hill *et al.* [12] and Liu *et al.* [13], by exploiting the two-dimensional (2-D) model proposed by Hocker [14], demonstrated that FBGs coated by materials with Young's modulus lower than that of the fiber glass may act as pressure sensors with enhanced sensitivity to the hydrostatic pressure. Their analyses were limited to the *hydrostatic* regime, and a *dynamical* extension to pressure acoustic waves is hitherto not available in the literature. From the experimental viewpoint, preliminary experimental studies by Cusano *et al.* [15,16] demonstrated that coated FBGs may outperform (in terms of acoustic sensitivity) standard uncoated configurations.

Against this background, in this paper, we carry out a systematic numerical analysis of the response of a coated FBG acting as an acoustic wave sensor. More specifically, we study the complex opto-acousto-mechanical interaction among an incident acoustic wave traveling in water, the optical fiber surrounded by the ring-shaped coating, and the FBG inscribed in the fiber, via full-wave numerical simulations by means of a multiphysics software package based on the finite-element method (FEM). In order to provide a full characterization of the sensor performance, we also carry out a comprehensive parametric analysis of the hydrophone sensitivity, by varying the geometrical and mechanical properties of the coating. Finally, we present a preliminary experimental validation.

The rest of the paper is structured as follows. In Section 2, the theoretical background underlying the operation of the underwater acoustic sensor is summarized, with particular reference to the acousto-mechanic interactions. Section 3 introduces the problem geometry, and provides some details on the simulation parameters and computational tools utilized throughout. Section 4 is devoted to the illustration and discussion of representative results

from harmonic and modal analysis. In Section 5, a preliminary validation of the proposed numerical analysis is presented, based on experimental data obtained by using polymeric coated FBG sensors. Finally, Section 6 contains some brief conclusions.

2. Theoretical background

The operational scenario of our underwater optical fiber hydrophone, schematically illustrated in Fig. 1, inherently involves a complex interplay of different physical phenomena.

Basically, when an acoustic wave propagating in water impinges on a solid object like the hydrophone, it acts as an external force onto the sensor external boundaries. The sensor's composite structure in turn undergoes a mechanical deformation according to its elastic properties. The resulting mechanical deformation (more specifically, the strain) on the FBG implies a Bragg wavelength shift proportional to the amplitude of the incident acoustic wave. In what follows, for the sake of the reader, we briefly review the main equations and related boundary conditions, which describe the underlying physical interactions, referring to topical textbooks [17,18] for a deeper analysis and further details. Throughout the paper, the water in which the acoustic waves propagate is modeled as a compressible ideal fluid, and is referred to as the “acoustic domain.” The hydrophone, which is a cylindrical composite structure constituted by an inner cylinder (optical fiber) and a ring-shaped overlay (coating), is modeled as a linear elastic medium, and is referred to as the “mechanical domain.”

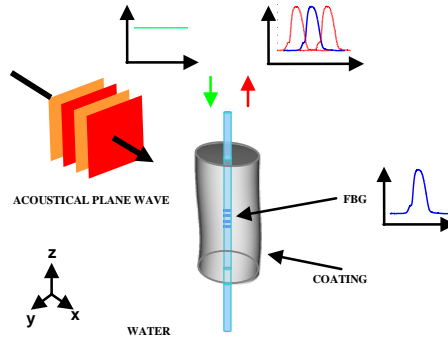


Fig. 1. Schematic description of the operational scenario for the underwater optical-fiber hydrophone (details in the text).

2.1 Acoustic domain: acoustic wave propagation

Acoustic waves are small perturbations (P, ρ) with respect to a constant equilibrium state (P_0, ρ_0) of a compressible ideal fluid [17], viz.,

$$(P', \rho') = (P, \rho) + (P_0, \rho_0), \quad (1)$$

where $P' = P'(t, x, y, z)$ and $\rho' = \rho'(t, x, y, z)$ are the scalar pressure field and the density of propagation medium, respectively, while $P = P(t, x, y, z) \ll P_0$ and $\rho = \rho(t, x, y, z) \ll \rho_0$ denote small perturbations with respect to the corresponding constant components P_0 and ρ_0 , respectively.

The propagation of pressure acoustic waves in compressible ideal fluids (e.g., water) is ruled by fundamental laws, known as the continuity equation and the Euler's equation respectively [17]:

$$\begin{aligned}\frac{\partial \rho}{\partial t} + \rho_0 \nabla \cdot \left(\frac{\partial \mathbf{U}}{\partial t} \right) &= 0, \\ \rho_0 \frac{\partial^2 \mathbf{U}}{\partial t^2} &= -\nabla P,\end{aligned}\tag{2}$$

where $\mathbf{U} = \mathbf{U}(t, x, y, z)$ is the displacement vector.

Sound waves in an ideal fluid are *adiabatic* [17], so that the pressure and density small perturbations are related via the equation

$$P = c^2 \rho,\tag{3}$$

where c is the speed of sound in the fluid. By combining Eqs. (2) and (3), we obtain the wave equation

$$\nabla^2 P - \frac{1}{c^2} \frac{\partial^2 P}{\partial t^2} = 0,\tag{4}$$

which, in the time-harmonic regime, yields the Helmholtz equation

$$\nabla^2 p + \left(\frac{\omega}{c} \right)^2 p = 0,\tag{5}$$

with ω denoting the angular frequency, and p denoting the frequency-domain pressure.

2.2 Mechanical domain: elastic wave propagation

In an elastic medium, waves propagate in the form of small oscillations of the stress field. The vector displacement \mathbf{U} in an elastic medium is described by the following elasto-dynamic equilibrium (Navier's) equation [18]:

$$\mu \nabla^2 \mathbf{U} + (\lambda + \mu) \nabla (\nabla \cdot \mathbf{U}) + \mathbf{F} = \rho'_s \frac{\partial^2 \mathbf{U}}{\partial t^2},\tag{6}$$

where \mathbf{F} is the dynamic load applied to the solid, ρ'_s the material density, and λ and μ the Lamè constants, which describe the elastic behavior of the medium and are related to the Young's modulus (E) and the Poisson's ratio (ν) via [18,19]

$$\lambda = \frac{\nu E}{(1+\nu)(1-2\nu)}, \quad \mu = \frac{E}{2(1+\nu)}.\tag{7}$$

Under the assumption of small deformations, the strains (Cartesian components) are related to the displacements by the linearized equation [18]

$$\varepsilon_{ij} = \frac{1}{2} \left(\frac{\partial U_i}{\partial j} + \frac{\partial U_j}{\partial i} \right),\tag{8}$$

with $i, j = x, y, z$. The strain tensor $\boldsymbol{\varepsilon}$ is related to the stress vector $\boldsymbol{\sigma}$ via the generalized Hooke's law [19]

$$\boldsymbol{\sigma} = \mathbf{D} \cdot \boldsymbol{\varepsilon},\tag{9}$$

where \mathbf{D} is the elastic constant matrix.

Finally, the elasto-dynamic equation governing the time-harmonic elastic wave propagation in a solid is given by [18]

$$\mu \nabla^2 \mathbf{u} + (\lambda + \mu) \nabla (\nabla \cdot \mathbf{u}) + \rho_s' \omega^2 \mathbf{u} = -\mathbf{f}, \quad (10)$$

where \mathbf{u} and \mathbf{f} are the frequency-domain displacement vector and the applied dynamic load, respectively.

2.3 Boundary conditions: acousto-mechanical interactions

In order to calculate the full response of the system, we need to connect the acoustic and mechanical domains via proper boundary conditions. Such conditions, enforced at the interface between the water domain and the cylindrical sensor may be summarized as follows [18]:

1. The normal displacement in the solid and fluid must be equal at the interface:

$$\rho_0 \omega^2 \mathbf{u} \cdot \mathbf{n} = \frac{\partial p}{\partial n}. \quad (11a)$$

2. The pressure must be in static equilibrium with the stress normal to the solid boundary:

$$\sigma_n = -p. \quad (11b)$$

3. In an ideal fluid, no tangential stresses must occur at the boundary:

$$\sigma_{\perp} = 0. \quad (11c)$$

In Eqs. (11a)-(11c), \mathbf{n} is the unit vector normal to the boundary surface, while σ_n and σ_{\perp} are the components of the stress vector normal and tangential to the boundary surface, respectively. Furthermore, within the mechanical domain, we assume perfect bonding between the optical fiber and the coating, which implies the additional boundary condition

4. The stresses and displacements at the fiber-coating interface must be continuous [17]:

$$\sigma_c = \sigma_f, \quad U_c = U_f, \quad (11d)$$

where the subscripts c and f identify the coating and fiber, respectively.

2.4 Optical domain

It is well known that an FBG is a strain sensor, and a mechanical deformation of the FBG results in a shift of the Bragg wavelength [7]. The relationship between strain and induced changes in the wavelength reflected in an FBG, normalized to its central wavelength, is given by [20]

$$\frac{\Delta \lambda}{\lambda_0} = \varepsilon_z - \frac{n_{eff}^2}{2} \left[p_{11} \varepsilon_x + p_{12} (\varepsilon_z + \varepsilon_y) \right], \quad (12)$$

where $\Delta \lambda$ is the Bragg wavelength shift, λ_0 is the central wavelength of the FBG, p_{11} and p_{12} are the elasto-optic parameters, n_{eff} is the effective refractive index, and ε_i ($i = x, y, z$) are the Cartesian strain components evaluated at the FBG location. It is noteworthy that Eq. (12) well describes the elasto-optic response of FBGs in most practical cases when no significant birefringence is induced ($\varepsilon_x = \varepsilon_y$), and the strain components are uniform along the FBG length [21]. The condition of uniformity of the strain components along the grating length is fulfilled when the acoustic wavelength is much larger than the FBG length [21], and when the border effects on the strain distribution, due to the composite cylinder ends, are negligible.

3. Problem geometry, observables, and methods

In our simulations, in order to model the *multi-physical* (acoustic and mechanical) interactions between an acoustic wave propagating in water and the composite structure constituting the hydrophone, we use the FEM-based commercial software package COMSOL Multiphysics® [22].

The underwater acoustic sensor under investigation is schematically represented by a 3-D structure (Fig. 2) composed by an inner cylinder (the optical fiber), with height h and radius R_f , and an outer annular cylinder (the ring shaped coating), with same height h and coating radius R_c . From the acousto-mechanical viewpoint, no distinction is made between the core and the cladding of the fiber. The sphere of radius R_w in Fig. 2 represents the water-filled acoustic domain surrounding the hydrophone.

Basically, the full-wave 3-D investigation of the acoustic-mechanical response of the underwater acoustic sensor, under the effect of a incident acoustic plane wave, is carried out in COMSOL by solving Eq. (5) in the acoustic domain, and by using the principle of virtual work (equivalent to the equilibrium equation in Eq. (10)) [22] in the mechanical domain. The resulting equations are coupled via the boundary conditions described in Eqs. (11). Moreover, at the spherical surface of the water domain, a radiation condition is set, so as to mimic an infinite water domain. At the external boundary, an acoustic plane wave (of amplitude $p_0 = 1\text{MPa}$) is set as a source. The analysis is carried out within the frequency range 0.5-30 kHz.

The FEM-based 3-D analysis yields the strain distribution ϵ along the x , y , and z axes into the optical fiber where the FBG is inscribed. The strain components evaluated at the FBG location $(x, y, z) = (0, 0, 0)$ are then used in the optical model to calculate the Bragg wavelength shift according to Eq. (12), whose conditions of applicability (cf. Section 2.4) are always fulfilled in the simulations below.

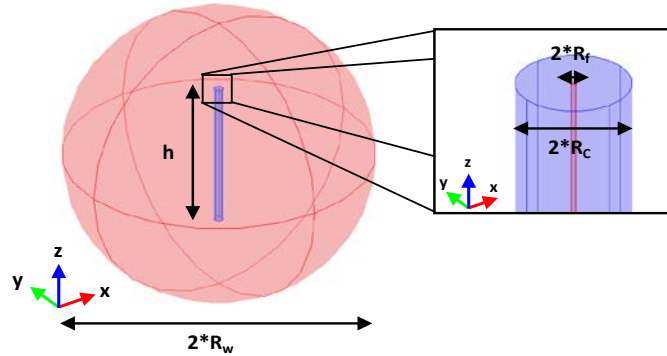


Fig. 2. 3-D geometry considered in the numerical simulations (details in the text).

The observable “sensitivity” can be defined as

$$S = \frac{\Delta\lambda}{\lambda_0 p_0} = \frac{1}{p_0} \left\{ \epsilon_z - \frac{n_{eff}^2}{2} \left[p_{11} \epsilon_x + p_{12} (\epsilon_z + \epsilon_y) \right] \right\}, \quad (13)$$

where $p_{11} = 0.121$, $p_{12} = 0.265$, and $n_{eff} = 1.465$ [12]. Moreover, from the ratio between the calculated sensitivity and that pertaining to the bare (i.e., uncoated) fiber in the hydrostatic case (following [12]), a sensitivity gain may be defined as

$$\text{Sensitivity Gain} = 20 \log_{10} \left(\left| \frac{S}{S_{BARE}} \right| \right), \quad (14)$$

where $S_{BARE} = -2.76 \cdot 10^{-6} \text{ MPa}^{-1}$ [12,14].

In order to gain a deeper insight into the sensor response and the underlying mechanisms, we also carried out a modal analysis, identifying the free vibration modes of the sensing structure. The analysis was still performed in COMSOL, by solving Eq. (10) in the absence of external loads [22].

For a comprehensive characterization of the sensor performance, we carried out a series of parametric studies, by varying the geometrical and physical parameters such as the coating height h , the coating radius R_c , the Young's modulus E , the Poisson's ratio ν , the density ρ' , and the loss factor η . In all the simulations below, we assume an optical fiber radius $R_f = 62.5 \mu\text{m}$, and an identical length h for the fiber and the coating. The remaining mechanical and acoustic parameters listed in Table 1 are kept constant.

The computational domain is discretized using a tetrahedral mesh. Numerical convergence was achieved for a discretization of at least five elements per acoustic wavelength. The simulations were performed by using the iterative Generalised Minimal Residual (GMRES) solver with the algebraic multi-grid pre-conditioner [22].

Table 1. Mechanical and Acoustic Constants of the Analyzed Structure

Parameter	Value
Optical fiber Young's modulus (E_f)	72 GPa
Optical fiber Poisson's ratio (ν_f)	0.17
Optical fiber density (ρ'_f)	2200 kg/m ³
Water density (ρ'_w)	997 kg/m ³
Speed of sound in water (c_w)	1480 m/s

4. Numerical analysis

4.1 Resonant behavior of the coated fiber Bragg gratings

In order to analyze the opto-acoustical response of our proposed sensor, we begin considering a specific configuration with fixed coating size and material properties, and investigate the interaction with an acoustic wave from the phenomenological viewpoint.

4.1.1 Harmonic analysis

The configuration of interest features a ring-shaped coating with an outer radius $R_c = 1.25 \text{ mm}$ (i.e., 20 times larger than the fiber radius) and a height $h = 4 \text{ cm}$. The elastic properties of the coating, given in Table 2, are consistent with the nominal properties of a specific thermosetting polyurethane (Electrolube UR5041) considered in [16]. The structure is excited by an acoustic plane wave normally-incident with respect to the cylinder axis. Numerical simulations are performed within the frequency range 500 Hz to 30 kHz (with steps of at least 1 kHz) of interest for typical SONAR applications. For all observables shown below, we also compute, as a reference, the zero-frequency values via the hydrostatic model [12,14].

Table 2. Elastic Properties of the Ring-Shaped Coating

Coating Parameters	Value
Young's modulus (E)	78 MPa
Poisson's ratio (ν)	0.3
Density (ρ')	1180 kg/m ³

Figure 3(a) shows the simulation results in terms of strain components along the x , y , and z axes over the whole frequency range of interest. Four sharp peaks are clearly visible in the strain components at frequencies 5.6, 14.8, 21.8 and 28.7 kHz. For better visualization of the background response (away from resonances) that is hidden by the strength of the resonant peaks, we show in Fig. 3(b) a magnified detail with the strain scale saturated. Similarly, in Fig. 3(c), we show a magnified detail around 14.8kHz, so as to illustrate with a finer sampling (down to 1Hz) the line-shape of the resonance. All the observed resonances clearly resemble the Fano line-shape and may be accurately fitted with a Fano-type model [23]. Recalling that Fano resonances stem from the interference between a *discrete* state with a *continuum* of states [23], we can infer that the resonances observed are attributable to the interaction between one of the vibration modes of the sensor and the impinging acoustic wave.

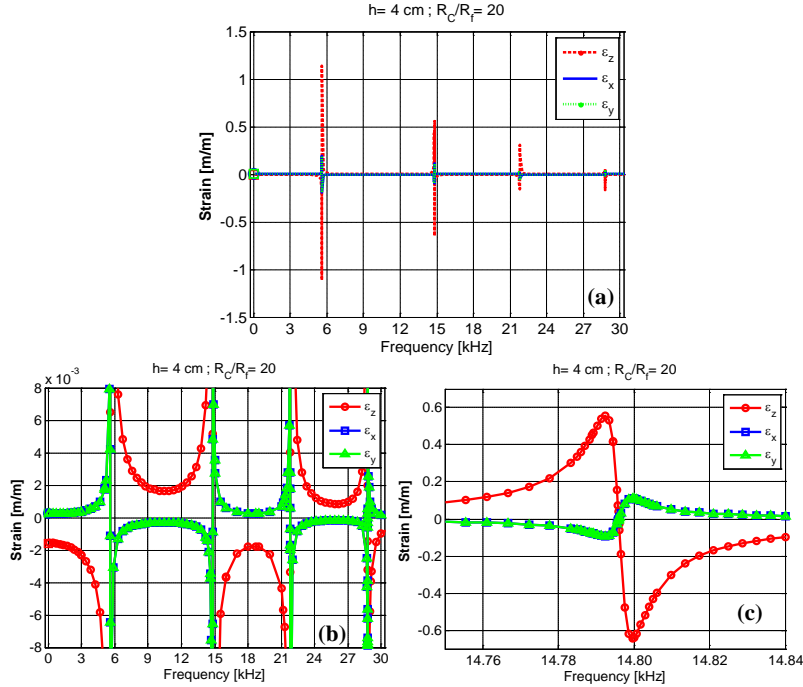


Fig. 3. (a) Spectra of the strain components (parameters detailed in the text). (b), (c) Magnified details along the strain and frequency axes, respectively.

As an illustration of the opto-acoustic response of the sensor to the impinging plane wave, Fig. 4 shows the pressure distribution in water (on the sphere boundary) and the z -strain distribution on the cylinder surface, for different frequencies (10, 20 and 30 kHz) away from resonances. As evident from Figs. 4(a-c), the cylindrical sensor responds to the impinging plane wave through a mechanical deformation, according to its elastic properties (see also the animation [Media 1](#)). The resulting strain at the FBG location determines a Bragg wavelength shift according to Eq. (12).

The sensitivity of this basic transduction principle is strongly enhanced at the resonant frequencies, where a Fano-type strain response occurs at the FBG location. In Fig. 4(d-e), we show the pressure distribution in water and the z -strain distribution on the cylinder surface around the second resonance (14.792 and 14.800kHz), with color scales suitably saturated so as to allow correct visualization of all distributions. From the pressure distribution, it can be observed the outgoing pressure radiated by the excited resonance (the discrete state) which, interfering with the impinging plane wave (the continuum), generates the Fano-resonance phenomenon.

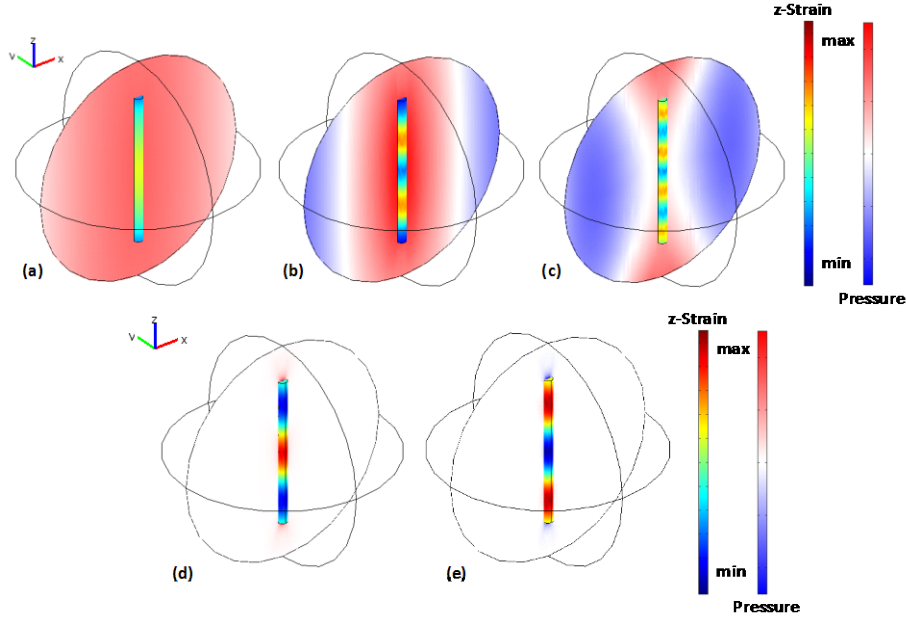


Fig. 4. Pressure distribution in water and z -strain distribution on the cylinder surface, for different frequencies of the acoustic wave (see also the animation [Media 1](#)), away from resonances: (a) 10 kHz, (b) 20 kHz, (c) 30 kHz, and around the second resonance: (d) 14.792 and (e) 14.800 kHz

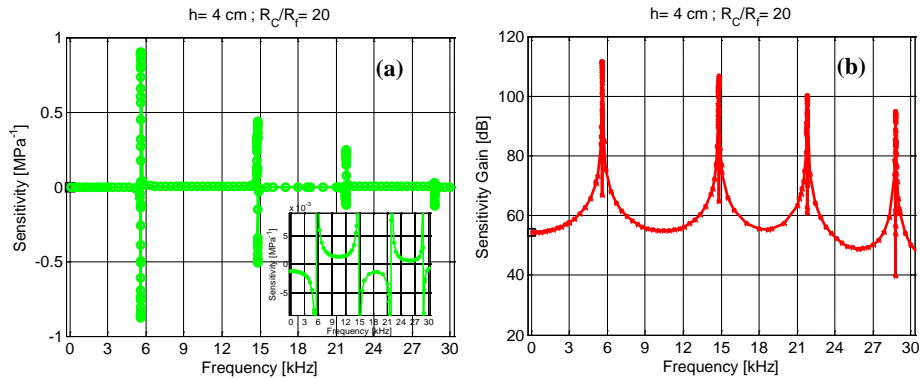


Fig. 5. (a) Sensitivity (cf. Eq. (13)) and (b) sensitivity gain (cf. Eq. (14)) spectra. The inset in (a) highlights the Fano-type line-shape of the sensitivity around the resonant frequencies.

Figures 5(a) and 5(b) show the sensitivity (cf. Eq. (13)) and corresponding sensitivity gain (cf. Eq. (14)), respectively, as a function of frequency, computed on the basis of the ε_x , ε_y , and ε_z strain distributions obtained from the simulations.

As expectable, at the resonant frequencies (5.6, 14.8, 21.8 and 28.7 kHz), the sensitivity also exhibits a resonant behavior, which retains the Fano-type line-shape (see the inset in Fig. 5(a)). The sensitivity gain in Fig. 5(b) is characterized by peaks of amplitude up to 110 dB, superimposed onto a ~ 50 dB background which is slowly decreasing with frequency.

Note that, in Fig. 5, the sensitivity value at zero-frequency computed via the hydrostatic model [12,14] is in very good agreement with our low-frequency predictions.

It is also worth noting that the high sensitivity values observed in Fig. 5 at the resonant frequencies strongly rely on the assumption of *zero damping* in the composite cylindrical structure, for which an excited resonance yields a *lossless* vibration. Moreover, the resonances

are *very narrow* (e.g., the sensitivity gain in Fig. 5(b) exceeds 80dB over bandwidths narrower than 0.5kHz).

To sum up, the numerical results above indicate that the ring-shaped coating is capable of significantly improving the sensitivity of the optical hydrophone, over the whole investigated frequency range, when compared with an uncoated FBG. Furthermore, the hydrophone sensitivity spectrum also exhibits characteristic resonant peaks, which yield a further strong enhancement.

4.1.2 Modal analysis

In order to identify the free vibration modes of the composite structure, and relate them with the sharp sensitivity resonances, we carried out a modal analysis of the optical hydrophone.

In particular, we computed the vibration modes of the composite cylindrical structure under investigation up to 30kHz. Figure 6 shows the only nonzero (z) component of the longitudinal resonant modes, visualized in terms of deformed shape (retrievable from the displacement vector) and strain distribution (in color scale). More specifically, the composite cylindrical structure of the sensor supports four longitudinal vibration modes (at frequencies 5.7, 15, 21.9 and 27.9kHz) characterized by *even* symmetry along the z -axis, and three longitudinal vibration modes (at frequencies 10.8, 18.7 and 25kHz) with *odd* symmetry along the z -axis. It is interesting to note that the sensitivity peaks observed in Fig. 5 occur at frequencies associated to the even modes only.

The comparison between the results from modal and harmonic analysis therefore confirms that the resonant features characterizing the hydrophone sensitivity are attributable to the excitation (by the normally-incident pressure plane wave) of longitudinal vibration modes with even symmetry. From the phenomenological viewpoint, this observation somehow resembles the excitation of guided resonances in periodic or quasi-periodic photonic crystals [24,25]. In fact, more in general, we observed that only the longitudinal vibration modes of the composite structure that exhibit a symmetry matching that of the impinging pressure plane wave are excited. In the normal-incidence case, only modes with even symmetry satisfy this condition (since plane waves exhibit even symmetry in the plane orthogonal to the direction of propagation) but, for *oblique* incidence, the excitation of vibration modes with odd symmetry becomes possible, as shown hereafter (see Section 4.3).

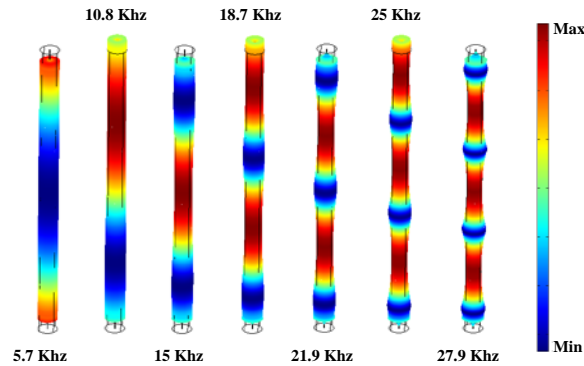


Fig. 6. Deformed geometry and z -strain distribution (in color scale) of the resonant modes.

As a concluding remark on this analysis, it should be noted that other vibration modes are supported by the composite structure (i.e., *bending* modes at frequencies 0.4, 1.0, 1.8, 2.9, 4.3, 5.7, 7.3, 9.0, 10.8, 12.7, 14.6, 16.5, 18.5, 20.5, 22.5, 24.5, 26.6 and 28.6kHz), which, however, do not give rise to sensitivity enhancements because they have intrinsically weaker longitudinal strain components with respect to the radial ones, and the Bragg wavelength is less sensitive to radial strain components with respect to the longitudinal one.

Moreover, for different physical and geometrical parametric configurations, other modes (of same and different kinds) may occur in the frequency range considered (e.g., *transversal*

modes may fall within the range if larger radii are assumed). Nevertheless, an exhaustive study of the natural frequencies of free-standing (and composite) elastic cylinders [26] is beyond the scope of this paper, which is instead focused on the effects induced by the excitation of such modes in the sensing performance.

4.2 Effects of the coating properties on the sensing performance

4.2.1 Size

We now move on to exploring the influence of the geometrical parameters of the structure (height and diameter) on the hydrophone frequency response, by maintaining the coating physical parameters fixed (see Table 2).

Figure 7 shows the sensitivity gain spectrum pertaining to a configuration with same radii as before, but with coating height $h = 1, 3$ and 4 cm. The response qualitatively resembles that in Fig. 5(b), with the number of resonant peaks changing with the cylinder height, and no significant changes in the background gain. In particular, the number of peaks tends to decrease when decreasing the height. From the modal analysis, the change in the number of sensitivity peaks is an effect of a frequency downshift occurring to the resonances when the cylinder height increases. Figure 8(a) illustrates such variation for the first three resonances: the resonant frequencies decrease with the coating height, and this decrease is faster for higher-frequency (e.g., third) peaks than for the lower-frequency (e.g., first) ones.

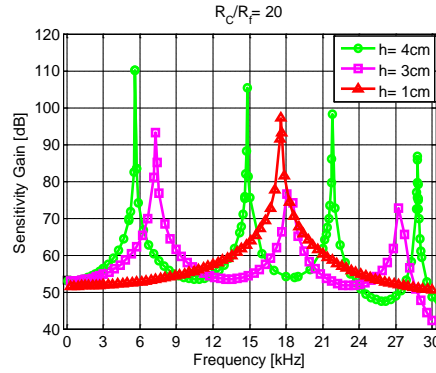


Fig. 7. Sensitivity gain spectra, for different coating heights.

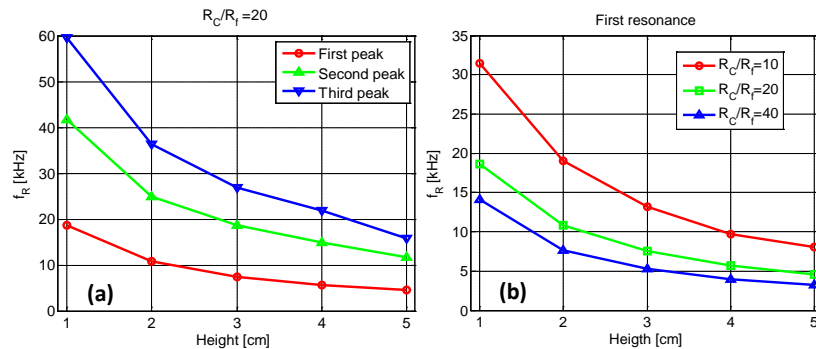


Fig. 8. (a) Resonant frequency as a function of coating height, for different peaks. (b) First resonant frequency as a function of coating height, for various coating radii.

In Fig. 8(b), with focus on the first resonance, we also show the effects of changing the coating radius ($R_C = 1.25, 2.5$ and 5 mm). By increasing the coating height, a decrease of the resonant frequency is still observed, and the slowest decrease is obtained for the largest coating radius.

Overall, regardless the coating radius, an increase of the height yields a decrease of the resonant frequencies, which eventually saturates. Consequently, the height of the ring-shaped coating may be a useful parameter for tuning the gain sensitivity peaks without affecting meaningfully the background sensitivity.

Figure 9 shows the sensitivity gain spectrum pertaining to a configuration with a fixed height $h = 4\text{ cm}$, and with coating radii $R_c = 0.625, 1.25, 1.875$ and 2.5 mm (i.e., ratios $R_c/R_f = 10, 20, 30$ and 40 , respectively), with the physical properties of the coating unchanged (Table 2). Some similarities and differences with respect to the previous case (changing the coating height) are worth highlighting. Similarly as before, the general spectral features (background with resonant peaks) are preserved when changing the coating radius, and the number of resonant peaks increases with increasing the radius. Figure 10(a) shows the variation of the first three resonant peak frequencies with the coating radius. Also in this case, a decrease of the resonant frequencies is observed, with the first peak moving slower than the third. In Fig. 10(b), we show the variation of the first resonant peak with the coating radius, for different height values. As can be observed, the fastest decrease is obtained for the smallest height considered. Basically, increasing the coating radius (similar to the coating height) yields a decrease of the resonant peak frequencies.

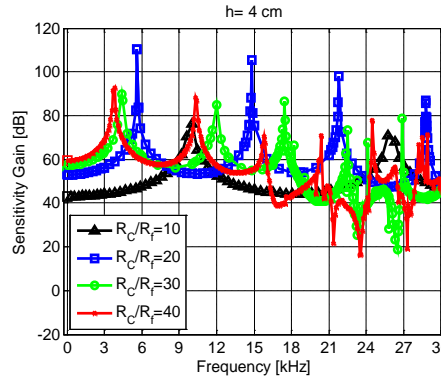


Fig. 9. Sensitivity gain spectra for different coating radii.

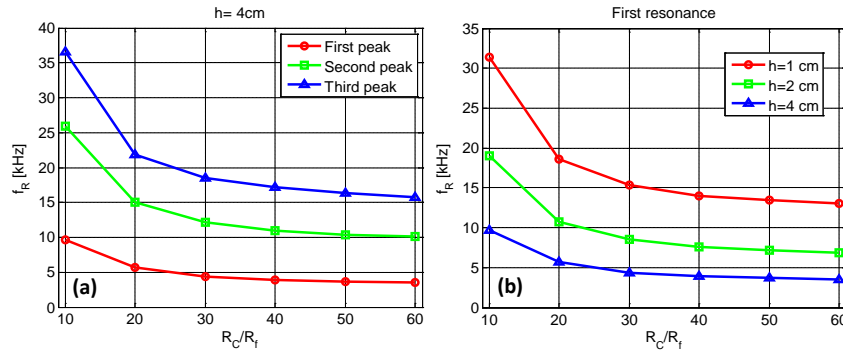


Fig. 10. (a) Resonant frequency as a function of coating radius, for various peaks. (b) First resonant frequency as a function of coating radius, for various coating heights.

All the variations of the resonant frequencies with the geometrical features of the ring-shaped coating were found to be in substantial agreement with the free vibration modes variations of a finite-length elastic composite cylinder [26].

Moreover, increasing the coating radius has two further main effects on the sensor performance: *i*) the enhancement of the background sensitivity at low frequencies, and *ii*) the progressive reduction of the background sensitivity at high frequencies.

In connection with the former effect, observing the low-frequency (below 3kHz) regions of the spectra in Fig. 9, it is evident that increasing the coating radius yields a significant enhancement of the sensitivity gain, up to a saturation value of about 60dB. To better highlight this aspect, in Fig. 11(a) we show the minimum values of the sensitivity gain between the first and second peaks, for various coating radii (up to $R_c/R_f = 60$). Basically, the sensitivity gain background increases with the coating radius until it reaches a constant value. This is in agreement with the hydrostatic model exploited in [12,14], and may be attributed to the role played by the ring-shaped coating in contrasting the stiffness of the optical fiber glass.

As for the latter effect, looking at the high-frequency (e.g., above 20 kHz, for $R_c/R_f = 40$) regions of the spectra in Fig. 9, an overall deterioration of the sensitivity gain can be observed, in spite of the appearance of additional resonances. In this framework, it is worth mentioning the appearance of *transversal* resonances (e.g., at 26.5 and 27.7 kHz for $R_c/R_f = 30$, and at 22.1 and 24.2kHz for $R_c/R_f = 40$) which, however, do not yield meaningful sensitivity enhancements. To highlight the deterioration of the sensitivity gain background, in Fig. 11(b) we show the spectra (extracted from Fig. 9) around the first local minima, from which a *low-pass* behavior is clearly observed, with a cut-off frequency that decreases when the coating radius increases, and the previously shown low-frequency gain level increasing with the coating radius. Note that such low-pass behavior could not be predicted by the hydrostatic model [12,14], and is attributable to diffraction effects occurring when the acoustic wavelength approaches the cylinder diameter.

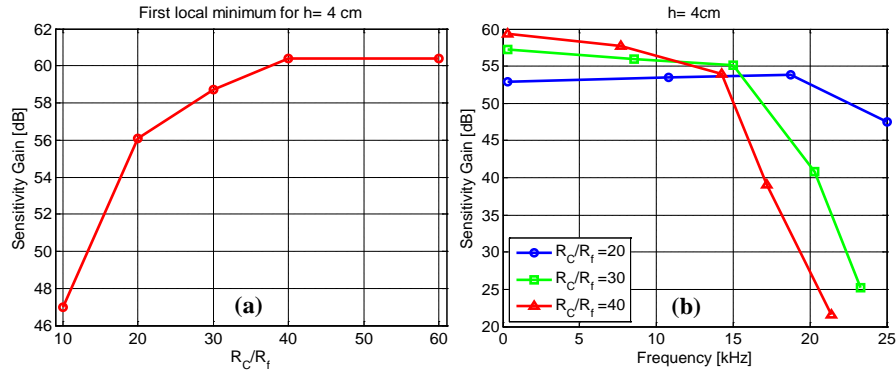


Fig. 11. (a) Sensitivity gain at first local minimum as a function of coating radius. (b) Sensitivity gain spectra around the first local minimum, for different coating radii.

4.2.2 Mechanical properties

In order to explore the effects of the coating elastic properties, we compared, for a given coating size ($h = 4$ cm and $R_c = 1.25$ mm), the sensitivities obtained by changing its Young's modulus E , Poisson's ratio ν , and density ρ' . The values used in the analysis are consistent with (but not strictly limited to) the nominal properties of certain specific polymeric materials (thermosetting polyurethanes), like that considered in [16], which are particularly suited to underwater applications in view of their adhesion (on the fiber glass) and waterproof properties.

We start by considering two basic materials: the former (identical to that considered so far, cf. Table 2) is characterized by $E = 78$ MPa, $\nu = 0.3$, and $\rho' = 1180$ kg/m³; the latter features the same Poisson's ratio, but $E = 970$ MPa and $\rho' = 1070$ kg/m³ (consistent with the thermosetting polyurethane Electrolube UR5528). Moreover, in order to separate the effects

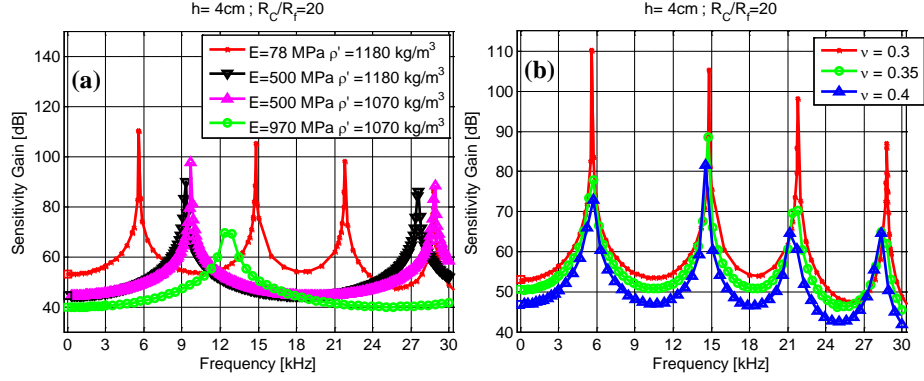


Fig. 12. Sensitivity gain spectra, by varying (a) the coating Young's modulus E and density ρ' (for $\nu = 0.3$), and (b) the coating Poisson's ratio ν (for $E = 78\text{ MPa}$ and $\rho' = 1180\text{ kg/m}^3$).

of the Young's modulus variation from those due to the density variation, we also consider other two sets of physical parameters (not corresponding to specific existing materials) featuring $E = 500\text{ MPa}$, $\nu = 0.3$, $\rho' = 1070\text{ kg/m}^3$, and $E = 500\text{ MPa}$, $\nu = 0.3$, $\rho' = 1180\text{ kg/m}^3$, respectively. Figure 12(a) shows the sensitivity-gain spectra pertaining to these four materials, from which it can be clearly seen that increasing the Young's modulus yields a desensitization of the hydrophone, accompanied by a high-frequency shift of the peaks. Much less significant are the effects of the density variations, limited to a slight sensitivity increase (for decreasing density) and frequency shift of the resonant peaks.

Finally, Fig. 12(b) illustrates the effects of the Poisson's ratio variations (from 0.3 to 0.4), for fixed $E = 78\text{ MPa}$ and $\rho' = 1180\text{ kg/m}^3$, which basically amount to a deterioration (for increasing values of ν) of the sensitivity-gain background (away from resonances), and a slight frequency shift of the resonant peaks.

Overall, the numerical results indicate that sensitivity enhancements may be obtained by using a ring-shaped coating characterized by low values of the Young's modulus, Poisson's ratio, and density. With reference to the Young's modulus and Poisson's ratio, this is in agreement with the hydrostatic analysis [12,14]. Basically, decreasing the Young's modulus and/or the Poisson's ratio reduces the bulk modulus K of the ring-shaped coating (given by $K = E / [3(1 - 2\nu)]$, for homogeneous, isotropic, linear elastic materials) which, for a given acoustic pressure, yields in turn an increase of the coating compression, and hence an enhancement of the strain components acting on the FBG. Further insight may be gained by considering the *characteristic acoustic impedance* Z of the material composing the ring-shaped coating, defined as [18]

$$Z = \rho' c_c = \rho' \sqrt{\frac{K}{\rho'}} = \sqrt{\frac{\rho' E}{3(1 - 2\nu)}}, \quad (15)$$

where c_c is the bulk speed of an elastic wave in a linearly-elastic solid. It can readily be noticed that the sensitivity optimization criteria emerged from the parametric analysis are consistent with a *minimization* of the coating impedance. It is also worth noting that such minimization implies an increase of the impedance mismatch with the surrounding water, which is detrimental in terms of increased signal reflection, but is largely compensated by the increase of the strain energy endowed to the FBG.

4.2.3 Structural damping

All the results discussed so far are obtained considering *lossless* materials. In what follows, we consider the effects of damping in both the glass fiber and the coating material. The structural damping is expressed in terms of a loss factor η defined as the ratio between the imaginary and real parts of the complex Young's modulus E [27]. Following [27], for the optical fiber, such loss factor assumed to be $\eta = 0.002$. Figure 13 illustrates the effects of damping with reference to a ring-shaped coating featuring $R_c/R_f = 20$, $h = 4$ cm, $\nu = 0.3$, $\rho' = 1180$ kg/m³, $\text{Re}(E) = 78$ MPa, and $\eta = 0.1$.

As expectable, it can be noted that the damping affects primarily the resonances (especially those at higher frequencies), yielding a strong sensitivity deterioration, while the baseline sensitivity gain turns out to be essentially unaffected. Since our model does not take into account the frequency-dependence of the coating elastic properties, the stronger deterioration effects observed at higher frequencies may be attributed to the corresponding longer acoustic paths in the coating. The effect of damping on the sensitivity must be carefully taken into account in the choice of the coating material, since a low Young's modulus (useful to increase the sensitivity, cf. Figure 12(a)) is often competing with a low damping, because "soft" materials typically exhibit high damping.

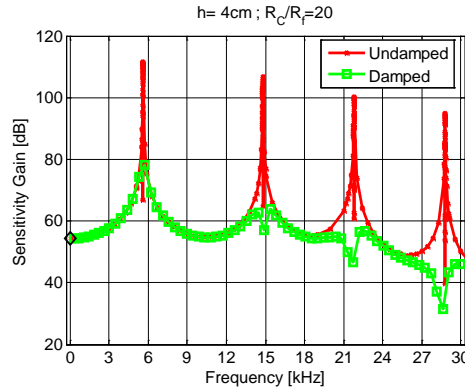


Fig. 13. Effects of the structural damping on the sensitivity gain spectrum, for a ring-shaped coating featuring ring-shaped coating featuring $R_c/R_f = 20$, $h = 4$ cm, $\nu = 0.3$, $\rho' = 1180$ kg/m³, $\text{Re}(E) = 78$ MPa, and $\eta = 0.1$.

4.3 Directivity

We conclude our parametric studies by considering the effects of *oblique* incidence, with specific reference to a parameter configuration featuring $R_c/R_f = 20$, $h = 3$ cm, $\nu = 0.3$, $\rho' = 1180$ kg/m³, $E = 78$ MPa, and no damping. In view of the cylindrical symmetry of the structure, we only consider variations of the angle θ between the incidence direction and the x - y plane. Thus, $\theta = 0$ represents the normal-incidence case considered so far, while for $\theta = \pi/2$ the acoustic wave travels parallel to the cylinder axis.

Figure 14(a) compares the sensitivity gain spectra for $\theta = 0$, $\pi/4$ and $\pi/2$. While the lower-frequency part of the spectrum turns out to be very weakly affected, at higher frequencies (above 9 kHz), the sensitivity gain visibly decreases for increasing incidence angles. This is better quantified in Fig. 14(b), which shows the sensitivity gain as a function of the incidence angle, at selected frequencies (3, 15 and 25kHz) away from resonances. Moving from normal ($\theta = 0$) to longitudinal incidence ($\theta = \pi/2$), the sensitivity gain gradually

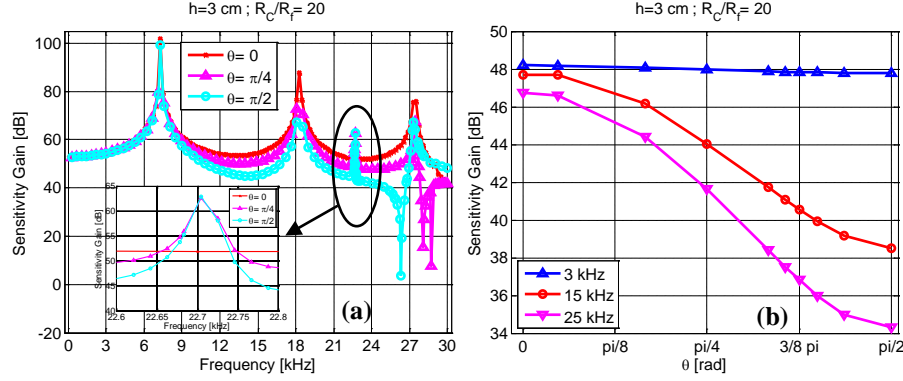


Fig. 14. (a) Sensitivity gain spectrum (magnified in the inset, around a resonant peak) pertaining to a ring-shaped coating featuring $R_c/R_f = 20$, $h = 3$ cm, $\nu = 0.3$, $\rho' = 1180$ kg/m³, $E = 78$ MPa, and no damping, for various sound-wave incidence directions. (b) Sensitivity gain angular response at selected frequencies.

deteriorates, and the higher frequencies turn out to be more affected. This is consistent with the dependence on the angle of incidence of the Rayleigh scattering from an elastic cylinder [28], and may therefore be simply attributed to the reduced cross-sectional area exhibited by the cylinder with respect to the wavelength of the impinging plane wave. In connection with the resonances, the first and the second peaks do not experience significant frequency shifts. The main difference between normal and oblique incidence (highlighted in the inset of Fig. 14(a)) consists in the appearance of a new (weaker) resonant peak at 22.7 kHz. The modal analysis indicates that such peak is attributable to a longitudinal *anti-symmetric* mode (odd z -strain distribution along the z -axis), which can be excited only under oblique incidence (see the discussion in Section 4.2.1).

5. Preliminary experimental validation

In order to validate the numerical modeling of the optical hydrophone, we carried out the experimental characterization of several coated FBGs in an instrumented water tank [29,30].

Here we report the preliminary results of the experimental characterizations in terms of sensitivity gain for two sensors, designed to operate efficiently at “low” frequencies (<15kHz) by means of Damival® E 13650 [31] coating (a polyurethane resin) and at “high” frequencies (15-30kHz) by means of Araldite® DBF [32] coating (an epoxy adhesive resin), respectively.

In particular, the optical hydrophones with Damival® and Araldite® are characterized both by a diameter of 5mm ($R_c/R_f = 40$), and a height of 3cm and 3.8cm, respectively.

Details on the setup for the experimental characterization can be found elsewhere [29,30]. Basically, a train of sine-wave pulses with duration 0.5ms at increasing frequencies in the range 4-30kHz (with step of 1kHz) is generated by an acoustic source immersed in the water tank, while reference data have been retrieved using a reference PZT hydrophone [30]. The FBG hydrophones were placed and maintained in vertical position by means of a few gram weight. Consequently, the sound pressure was perpendicular to the fiber longitudinal axis. For each frequency, the resulting time responses of the coated FBGs sensors to the acoustic excitation were measured via a tunable laser locked to work at the edge of the FBG spectra [30]. From the time responses (corresponding to the acoustical sine-wave pulses), the amplitudes of optical sensor responses have been obtained through FFT analysis and used to reconstruct the sensitivity curve vs. frequency.

The obtained experimental sensitivity gains are reported in Fig. 15 (a-b). In the same plots the corresponding numerical predictions are also shown for comparison. A good agreement between the experimental data and the numerically predicted sensitivity gains can be

Table 3. Properties of the Ring-Shaped Coatings

Elastic Properties	Nominal Range		Estimated Values	
	Polyurethane resins	Araldite®	Damival® E 13650	Araldite® DBF
Young's modulus (E)	69-690MPa [33]	2.6-3.7GPa [36]	200MPa	2.9GPa [30]
Poisson's ratio (ν)	0.3-0.49 [34]	0.324-0.345 [36]	0.4	0.345
Loss Factor (η)	0.05-0.5 [35]	$1 \cdot 10^{-2}$ - $1 \cdot 10^{-1}$ [37]	0.1	$2 \cdot 10^{-2}$
Density (ρ')	1030-1500 kg/m ³ [33]	1000-1850 kg/m ³ [38]	1180 kg/m ³	1100 kg/m ³ [30]

clearly observed. It is worth noting that the elastic properties of the polymeric coatings used to numerically reconstruct the experimental data are consistent with those found in literature for both class of materials: polyurethane resins for Damival® E 13650 and Araldite® based resins for Araldite® DBF, as observable in Table 3. This last evidence and the good agreement observed clearly demonstrate the correctness of the proposed numerical modeling as well as its prediction capability.

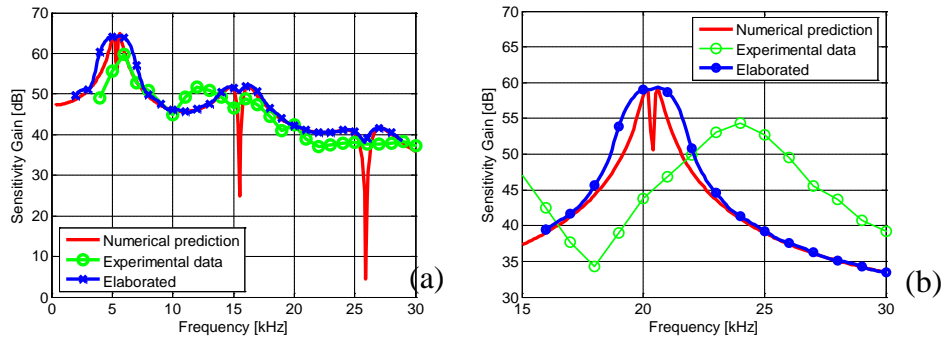


Fig. 15. Numerical and experimental sensitivity gain of a coated FBG respect to bare fiber vs frequency (a) with the Damival® E 13650 coating and (b) with the Araldite® DBF coating. “Elaborated” data take into account the finite duration of the acoustic pulse

The comparison primarily confirms the resonant behavior of the underwater acoustic sensor outlined by the numerical analysis, which in turn demonstrates to be able to supply physical insight in the sensor operation and at the same time to offer acceptable prediction capabilities both in terms of resonant frequencies and sensitivity values.

The disagreements between experimental and numerical data (particularly evident with the Araldite® coating) can be attributed to second order effects (physical imperfections, acoustically induced particle fluid motion, etc.), which have not been taken into account in the simulations, but that are not able to dominate the basic transduction mechanism.

A major difference between the experimental and numerical data can be found in the shape of the sensitivity gain peaks. Differently from the experimental observations, the numerical predicted Fano line shape in the sensitivity would imply a zero crossing for the sensitivity and thus a narrow dip in the sensitivity gain for each resonance (actually the dip is well observable in the numerical plots only when a fine frequency sampling is employed).

From the experimental viewpoint, these narrow spectral features cannot be observed due to the finite duration of a single acoustic tone (0.5ms) limiting the spectral resolution of the experimental characterization (in turn experimentally the pulse duration is limited in order to avoid the superposition of the direct wave with the reflected ones in the tank). To better explain the effect of the limited spectral resolution on the numerical predictions, in Fig. 15(a-b) we show (with the trace “elaborated”) the numerical sensitivity gain accounting for the finite duration of the acoustic pulse. It is evident in Fig. 15 that the finite time extent of the sine wave pulses smoothes the sharp spectral features by strongly deemphasizing the presence of the narrow dips and justifying the difference between numerical and experimental data in

the peaks shapes when this effect is not taken into account. Finally, further analysis is currently under way to improve the correlation between numerical and experimental data.

6. Conclusions

In summary, we have reported the first evidence of the resonant behavior of an underwater acoustic sensor constituted by an FBG coated by a ring-shaped material. We have carried out a full 3-D numerical analysis of this acoustic sensor in the frequency range 0.5-30 kHz, thereby extending previous studies on coated FBGs [12] limited to approximate hydrostatic modeling.

Our numerical results fully characterize the opto-acoustic response of the optical hydrophone, and indicate that the coating may significantly enhance the sensitivity over the whole investigated frequency range, by comparison with an uncoated FBG. The excitation of characteristic resonances (at frequencies related to the physical and geometrical parameters) of the cylindrical coating further improves the sensor performance. With the aid of modal analysis, we have associated the frequency peaks with longitudinal vibration modes supported by the coating. In particular, under normally-incident plane wave excitation, the structure exhibits sensitivity peaks associated to symmetric longitudinal modes, whereas anti-symmetric modes may also be excited under oblique incidence.

The results from our comprehensive parametric studies also indicate that the coating height and radius may be effectively utilized in order to tune the resonant frequencies. Furthermore, larger coating radii may be beneficial in improving the low-frequency background sensitivity, but detrimental in the high-frequency region. In connection with the coating elastic properties, low values of the Young's modulus, Poisson's ratio, and density are desirable for enhancing the sensitivity, and the detrimental effect of structural damping on the resonant peaks needs to be carefully accounted for.

Several aspects emerged from this study (e.g., the resonant behavior of the acoustic sensor, as well as the diffraction-related effects of the radius increase) could have not been predicted by the hydrostatic model utilized in [12,14]. Our full-wave numerical analysis, besides providing a physical insight in the interaction between the impinging acoustic wave and the sensor, also gives useful hints and guidelines for the design and performance optimization towards specific applications. For instance, the resonant behavior can be better exploited in active acoustic sensing applications whereas the sensor behavior in a frequency range away from the resonances seems better suited for passive acoustic sensing.

Finally, a preliminary validation of the proposed numerical analysis has been carried out through experimental data obtained using polymeric coated FBGs sensors. As a matter of fact, a good agreement between the experimental characterizations and the numerically predicted sensitivity gains has been obtained, confirming the correct modeling of the hydrophone as well as its prediction capability.

Acknowledgments

We would like to acknowledge Dr. Marco Consales and Dr. Agostino Iadicicco for their kind support and active collaboration in the experimental measurements and the Whitehead Alenia Sistemi Subacquei (WASS) for the availability of the instrumented water tank.